

Which curvature is right for you? Part - 2

Satinder Chopra*, Arcis Seismic Solutions, Calgary, Alberta, Canada

schopra@arcis.com

and

Kurt J. Marfurt, The University of Oklahoma, Norman, Oklahoma, US.

Introduction

The conventional computation of curvature may be termed as structural curvature, as lateral second-order derivatives of structural component of seismic time or depth of reflection events are used to generate them. Here, we explore the case of applying lateral second-order derivatives on the amplitudes of seismic data along the reflectors. We refer to this second computation as amplitude curvature. For volumetric structural curvature we compute first-derivatives of the volumetric inline and crossline components of structural dip. For amplitude curvature we apply a similar computation to the volumetric inline and crossline components of the energy-weighted amplitude gradients, which represent the directional measures of amplitude variability. Since the amplitude and structural position of a reflector are mathematically independent properties, application of amplitude curvature computation to real seismic data often shows different, and sometimes more detailed illumination of geologic features than structural curvature. However, many features, such as the delineation of a fault where we encounter both a vertical shift in reflector position and a lateral change in amplitude, will be imaged by both attributes, with images 'coupled' through the underlying geology.

Geometric attributes such as coherence and curvature are useful for delineating a subset of seismic stratigraphic features such as shale dewatering polygons, injectites, collapse features, mass transport complexes and overbank deposits, but have limited value in imaging classic seismic stratigraphy features such as onlap, progradation and erosional truncation. In this context, we review the success of current geometric attribute usage and discuss the applications of newer volumetric attributes such as reflector convergence and reflector rotation about the normal to the reflector dip. While the former attribute is useful in the interpretation of angular unconformities, the latter attribute determines the rotation of fault blocks across discontinuities such as wrench faults. Such attributes can facilitate and quantify the use of seismic stratigraphic workflows to large 3D seismic volumes.

Algorithm description

Structural curvature requires the (explicit or implicit) computation of lateral second derivatives of reflector time or depth. Many processing geophysicists focused on statics and velocity analysis think of seismic data as composed of amplitude and phase components, where the phase associated with any time t and frequency f is simply $\phi=2\pi f t$. Indeed, several workers have used

the lateral change in phase as a means to compute reflector dip (e.g. Scheuer and Oldenburg, 1988; Barnes, 2000; Marfurt and Kirlin, 2000).

We can also compute second derivatives of amplitude (Figure 1). Horizon-based amplitude curvature is in the hands of most interpreters. First, one generates a horizon slice through a seismic amplitude, RMS amplitude, or impedance volume, $a(t,x,y)$. Next, one computes the inline ($\partial a/\partial x$) and crossline ($\partial a/\partial y$) derivatives of this map. Such maps can often delineate the edges of bright spots, channels, and other stratigraphic features at any desired direction, ξ , by combining the two measures with simple trigonometry

$$\frac{\partial a}{\partial \xi} = \cos \xi \frac{\partial a}{\partial x} + \sin \xi \frac{\partial a}{\partial y} . \quad \dots\dots\dots(4)$$

A common edge detection algorithm is to compute the Laplacian of a map (though more of us have probably applied this filter to digital photographs than to seismic data),

$$e_{mean} = \frac{1}{2} \nabla^2 a = \frac{1}{2} \left(\frac{\partial^2 a}{\partial x^2} + \frac{\partial^2 a}{\partial y^2} \right) \dots\dots\dots(5)$$

Equation 5 is the formula for the mean amplitude curvature.

Luo *et al.* (1996) showed that if one were to first estimate structural inline and crossline dip, that one can generate an excellent edge detector that is approximately

$$C_{Sobel} = \left\{ \frac{\sum_{k=-K}^{+K} \left(\left[\frac{\partial a_{jk}}{\partial x} \right]^2 + \left[\frac{\partial a_{jk}}{\partial y} \right]^2 \right)_{j=center}}{\sum_{k=-K}^{+K} \sum_{j=1}^J a_{jk}^2} \right\}^{1/2} \dots\dots\dots(6)$$

where the derivatives are computed in a $(-K$ to $+K$ vertical sample, J -trace) analysis window oriented along the dipping plane and the derivatives are evaluated at the center of the window. Marfurt and Kirlin (2000) and Marfurt (2006) showed how one can compute accurate estimates of reflector amplitude gradients, \mathbf{g} , from the KL-filtered (or principal component of the data) within an analysis window:

$$g_x = \lambda_1 \sum_{k=-K}^{+K} \frac{\partial v_1(x,y)}{\partial x}, \text{ and} \\ g_y = \lambda_1 \sum_{k=-K}^{+K} \frac{\partial v_1(x,y)}{\partial y}, \quad \dots\dots\dots 7)$$

where \mathbf{v}_1 is the principal component or “eigenmap” of the amplitude within a J -trace analysis window, and λ_1 is its corresponding eigenvalue, which represents the energy of this data component.

In Figures 2A and B we show the images for 3D chair views of a vertical slice through the seismic amplitude volume correlated with the inline and crossline amplitude gradients. Both images express independent views of the same geology (almost N-S oriented main faults and fault related fractures) much as two orthogonal shaded illumination maps.

Geological structures often exhibit curvature of different wavelengths such that structural curvature images of different wavelengths provide different perspectives of the same geology (Bergbauer *et al.*, 2003; Al-Dossary and Marfurt, 2006). The authors of this paper have presented many applications of such multispectral estimates of curvature from seismic data (Chopra and Marfurt, 2006, 2007a and b, 2010). Short wavelength curvature often delineates details with intense highly localized fracture systems. Long wavelength curvature on the other hand enhances subtle flexures on a scale of 100-200 traces that are difficult to see on conventional seismic data, but are often correlated to fracture zones that are below seismic resolution as well as to collapse features and diagenetic alterations that result in broader bowls.

Application

In Figure 3 we show a comparison of the long- and short-wavelength computation of most-positive and most-negative amplitude and structural curvature measures. We notice that for both long and short wavelength, the amplitude curvature estimates provide additional information. Structural most-positive curvature displays in Figure 3B and D show lower frequency detail as compared with their equivalent amplitude curvature displays in Figures 3A and C.

Volumetric estimates of seismic reflector rotation and convergence

Algorithm description

Seismic stratigraphic analysis refers to the analysis of the configuration and termination of seismic reflection events, packages of which are then interpreted as stratigraphic patterns. These packages are then correlated to well-known patterns such as toplap, onlap, downlap, erosional truncation, and so forth, which in turn provide architectural elements of a depositional environment (Mitchum *et al.*, 1977). Through well control as well as modern and paleo analogues, we can then produce a probability map of lithofacies.

Geometric attributes such as coherence and curvature are commonly used for mapping structural deformation and depositional environment. Coherence proves useful for identification of faults, channel edges, reef edges and collapse features while curvature images folds, flexures, sub-seismic conjugate faults that appear as drag or folds adjacent to faults, roll-over anticlines, diagenetically altered fractures, karst and differential compaction over channels.

While coherence and curvature are excellent at delineating a subset of seismic structural and stratigraphic features they have only limited value in imaging classic seismic stratigraphy features such as onlap, progradation, erosional truncation, and reflector rotation about a fault. The progradations may look smooth and relatively coherent, except at locations where they intersect a

bounding surface. By construction, curvature quantitatively measures the strength of structural features that can be represented by quadratic surfaces: dome, ridges, saddles, valleys, bowls, and when there is no deformation, planes. Due to the distinct change in reflector dip and/or terminations, erosional unconformities and in particular angular unconformities are relatively easy to recognize on vertical seismic sections. Although there will often be a low-coherence anomaly where reflectors of conflicting dip intersect, these anomalies take considerable skill to interpret. Barnes (2000) was perhaps the first to discuss the application of attributes based on the description of seismic reflection pattern and used them to map angular unconformities amongst other features. As the first step he computed volumetric estimates of vector dip. Next, the mean and standard deviation of the vector dip are calculated in narrow windows. Parallel reflectors exhibit a smaller standard deviation than non-parallel reflectors such as angular unconformities.

Computing a vertical derivative of apparent dip at user-defined azimuth, Barnes (2000) also defined the convergence/divergence of reflections. Convergent reflections would show a decreasing dip with depth/time at constant azimuth. Marfurt and Rich (2010) built upon Barnes' (2000) method by taking the curl of the volumetric vector dip thereby generating a 3D reflector convergence azimuth and magnitude estimates.

Compressive deformation and wrench faulting cause the fault blocks to rotate (Kim *et al.*, 2004). Such rotation has been observed in laboratory measurements. The extent of rotation depends on the size, the comprising lithology and the stress levels. As the individual fault blocks undergo rotation, it is expected that the edges experience higher stresses and undergo fracturing.

Natural fractures are controlled by fault block rotation and depend on how the individual fault segments intersect. Fault block rotation can also control depositional processes by providing increased accommodation space in subsiding areas and erosional processes in uplifted areas. In view of this importance of the rotation of the fault blocks, a seismic attribute application focusing on the rotation of the fault blocks is required. Besides the reflector convergence attribute mentioned above, Marfurt and Rich (2010) also discuss the calculation of another attribute that determines the rotation about the normal to the reflector dip and would be a measure of the reflector rotation across a discontinuity such as a wrench fault.

As the first step, the inline and crossline components of dip are determined at every single sample in the 3D volume using semblance search or any other available method. After defining the three components of the unit normal, \mathbf{n} , and the rotation vector $\boldsymbol{\psi}$, Marfurt and Rich (2010) define the rotation about the normal to the reflector dip as

$$r = \mathbf{n} \bullet \boldsymbol{\psi} = n_x \left(\frac{\partial n_y}{\partial z} - \frac{\partial n_z}{\partial y} \right) + n_y \left(\frac{\partial n_z}{\partial x} - \frac{\partial n_x}{\partial z} \right) + n_z \left(\frac{\partial n_x}{\partial y} - \frac{\partial n_y}{\partial x} \right) \dots \dots \dots (2)$$

which is essentially a measure of the reflector rotation across a discontinuity such as a wrench fault. If average reflector is perfectly flat, only the term multiplying $n_z=1$ contributes which measures rotation about the vertical axis, which is mathematically the change of the inline dip in the crossline direction minus the change of the crossline dip component in the inline direction.

Similarly, Marfurt and Rich (2010) compute reflector convergence as follows:

$$\begin{aligned}
 \mathbf{c} = \mathbf{n} \times \boldsymbol{\psi} = & \hat{\mathbf{x}} \left[n_y \left(\frac{\partial n_x}{\partial y} - \frac{\partial n_y}{\partial x} \right) - n_z \left(\frac{\partial n_y}{\partial z} - \frac{\partial n_z}{\partial y} \right) \right] \\
 & + \hat{\mathbf{y}} \left[n_z \left(\frac{\partial n_y}{\partial z} - \frac{\partial n_z}{\partial y} \right) - n_x \left(\frac{\partial n_x}{\partial y} - \frac{\partial n_y}{\partial x} \right) \right] \\
 & + \hat{\mathbf{z}} \left[n_x \left(\frac{\partial n_x}{\partial x} - \frac{\partial n_z}{\partial z} \right) - n_y \left(\frac{\partial n_y}{\partial z} - \frac{\partial n_z}{\partial y} \right) \right]
 \end{aligned}
 \tag{3}$$

Again, if the average reflector is perfectly flat, only the terms multiplying $n_z=1$ contribute, with the one that multiplies the unit vector in \mathbf{x} representing the rotation about the \mathbf{x} axis (or convergence/divergence in the y - z plane), and the that one multiplies the unit vector in \mathbf{y} representing rotation about the \mathbf{y} axis (or convergence/divergence in the x - z plane).

Application

Note that the reflector convergence, \mathbf{c} , is a vector consisting of a magnitude and azimuth. We use a 2D color wheel to display such a result, where parallel reflectors (magnitude of convergence = 0) appear as white, and the azimuth of convergence is mapped against a cyclical color bar, with the colors becoming darker for stronger convergence. Figure 6 shows a suite of cartoons of a channel with or without levee/overbank deposits, in terms of the following cases:

Figure 4A where the deposition within the channel shows no significant convergence;

Figure 4B where the deposition within the channel is such that the west channel margin is converging towards the west and the east channel margin is converging towards the east. This is displayed in color to the right with the help of a 2D color wheel;

Figure 4C where the deposited sediments within the channel are not converging at the margins, but the levee/overbank deposits converge towards the channel (west deposits converge towards the east and vice-versa; and

Figure 4D where both the strata within the channel and levee/overbank deposits are converging. This appears to be a combination of Figure 6B and C above.

Notice how the convergence shows up in color (using the 2D color wheel) as displayed to the right in cyan and magenta colors along the channel edges.

We carried out the computation of reflector convergence and the rotation about the normal to the reflector dip attributes for a suite of 3D seismic volumes from Alberta, Canada. Figure 5 depicts a 3D chair view with a coherence time slice exhibiting a channel system, co-rendered with reflector convergence attribute using a 2D color wheel. Within the area highlighted by the ellipse in yellow dotted line, an interpretation has been made keeping in mind the cases shown in Figure 4. Apparently, the levee/overbank deposit converging towards the channel margin generating the magenta and green colors with respect to the reflector convergence.

In Figure 6 a 3D chair display with the vertical inline and crossline displays and a time slice through the reflector rotation about the average reflector normal volume. Notice the horst and graben features show considerable contrast so as to be conveniently interpreted. An equivalent

display is shown in Figure 7, but with the time slice from the reflector convergence attribute. The display uses a 2D color wheel wherein the blue color indicates reflectors pinching out to the North, red to the Southeast and cyan to the Northwest.

Conclusions

Reflector convergence and the reflector rotation about the normal to the reflector dip are two recently-developed attributes. Applications to a channel system from Alberta, Canada, provide a means to quantitatively measure and visualize thickening and thinning associated with an incised valley system and its associated levee and overbank deposits. Application to a horst and graben system provides a means to quantitatively measure and visualize syntectonic deposition and/or erosion within the fault blocks, as well as dip-slip rotation about the fault.

Reflector-convergence based attributes do not delineate unconformities and nonconformities exhibiting near parallel reflector patterns. Condensed sections are often seen as stratigraphically parallel low-coherence anomalies on vertical sections. More promising solutions to mapping these features are based on changes in spectral magnitude components (Smythe *et al.*, 2004) or in spectral phase components (Castro de Matos *et al.*, 2011).

For data processed with an amplitude preserving sequence, amplitude variations are diagnostic of geologic information such as changes in porosity, thickness and /or lithology. Computation of curvature on amplitude gradients provides a means to delineate tuning features associated with pinchouts, and amplitude anomalies associated with diagenetic alteration of faults and joints. The application of amplitude curvature to impedance images is particularly promising (Guo *et al.*, 2010).

References

- Al-Dossary, S., and K. J. Marfurt, 2006, Multispectral estimates of reflector curvature and rotation: *Geophysics*, v. 71, p. P41-P51.
- Barnes, A. E., 2000, Attributes for automated seismic facies analysis: 70th Annual International Meeting, SEG, Expanded Abstracts, p. 553-556.
- Bergbauer, S., T. Mukerji, and P. Hennings, 2003, Improving curvature analyses of deformed horizons using scale-dependent filtering techniques: *AAPG Bulletin*, v. 87, p. 1255-1272.
- Castro de Matos, M., O. Davogustto, K. Zhang, and K. J. Marfurt, 2011, Detecting stratigraphic discontinuities using time-frequency seismic phase residues, *Geophysics*, v. 76, p. P1-P10.
- Chopra, S., and K.J. Marfurt, 2007a, *Seismic Attributes for Prospect Identification and Reservoir Characterization*, book under production by SEG.
- Chopra, S. and K.J. Marfurt, 2007b, Curvature attribute applications to 3D seismic data, *The Leading Edge*, v. 26, p. 404-414.
- Chopra, S. and K.J. Marfurt, 2000, Integration of coherence and curvature images, *The Leading Edge*, v. 29, p. 1092-1107.
- Guo, Y., K. Zhang, and K.J. Marfurt, 2010, Seismic attribute illumination of Woodford Shale faults and fractures, Arkoma Basin, OK: 80th Annual International Meeting of the SEG, Expanded Abstracts, p. 1372-1376.
- Kim, Y. S., D.C.P. Peacock, and D.J. Sanderson, 2004. Fault damage zones: *Journal of Structural Geology*, v. 26, p. 503-517.
- Luo, Y., W. G. Higgs, and W. S. Kowalik, 1996, Edge detection and stratigraphic analysis using 3-D seismic data: 66th Annual International Meeting, SEG, Expanded Abstracts, 324-327.
- Marfurt, K.J., and R.L. Kirlin, 2000, 3D broadband estimates of reflector dip and amplitude: *Geophysics*, v. 65, p. 304-320.

Marfurt, K.J. and J. Rich, 2010, Beyond curvature – volumetric estimates of reflector rotation and convergence, 80th Annual International Meeting, SEG, Expanded Abstracts, p. 1467-1472.

Mitchum, R.M. Jr., P.R. Vail, and J.B. Sangree, 1977, Seismic stratigraphic and global changes of sea level: part 6. Stratigraphic interpretation of seismic reflection patterns in depositional sequences: section 2. Application of seismic reflection configuration to stratigraphic interpretation: AAPG Special volumes, Memoir 26, p. 117-133.

Roberts, A., 2001, Curvature attributes and their application to 3D interpreted horizons. The First Break, v. 19, p. 85-99.

Scheuer, T.E. and D.W. Oldenburg, 1988, Local phase velocity from complex seismic data: Geophysics, v. 53, p. 1503-1511.

Smythe, J., A. Gersztenkorn, B. Radovich, C.-F. Li, and, C. Liner, 2004, SPICE: Layered Gulf of Mexico shelf framework from spectral imaging: The Leading Edge, v. 23, p. 921-926.

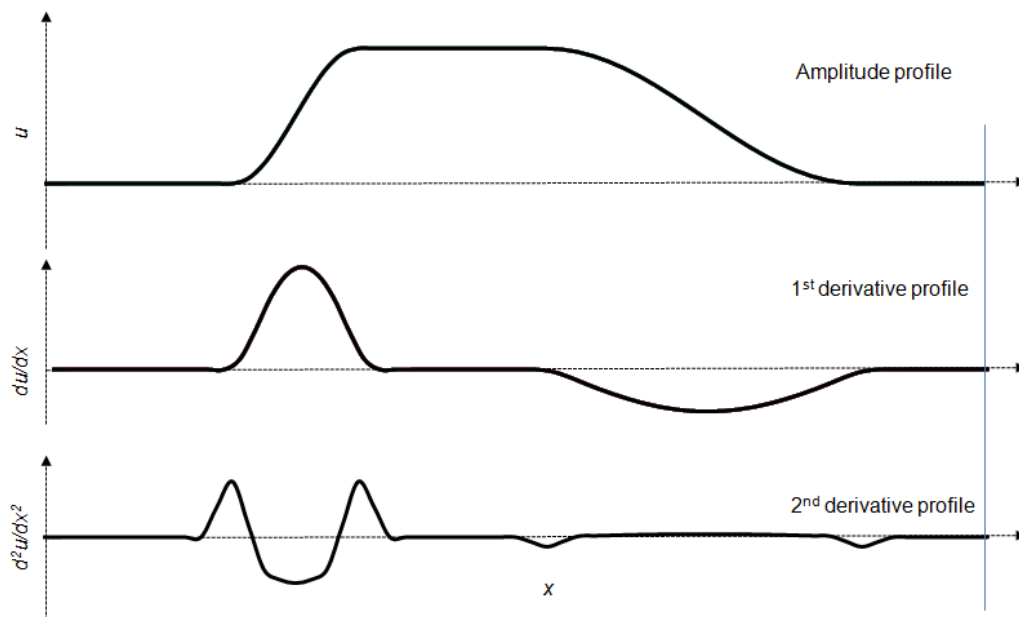


Figure 1. Effect of the first and second derivative on a one-dimensional amplitude profile. The two extrema seen in the 2nd derivative shows the limits of the amplitude anomaly.

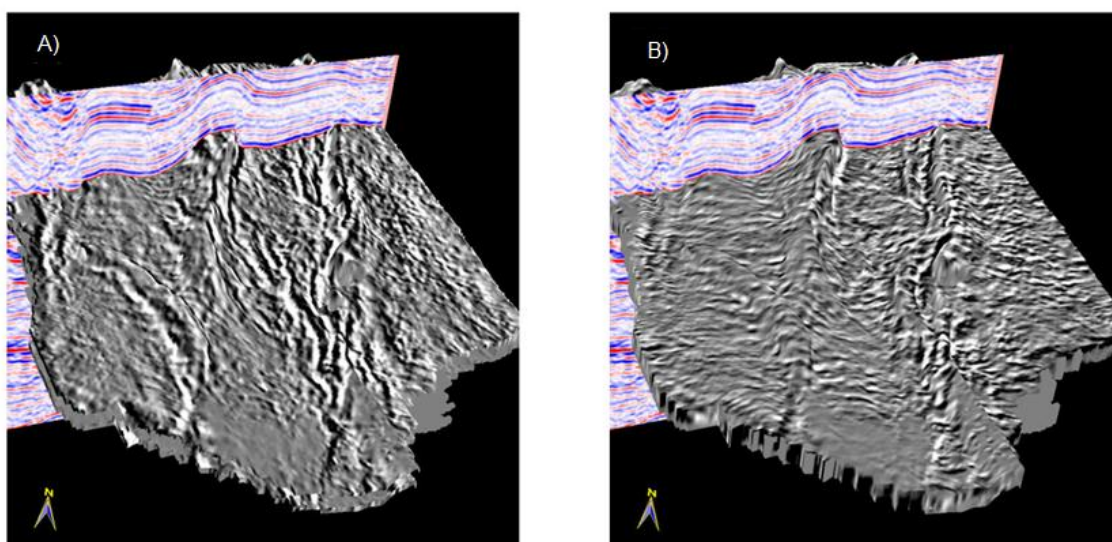


Figure 2. 3D chair view showing the seismic inlines correlated with (A) inline-energy gradient and (B) crossline energy gradient strat cubes. Each strat-cube exhibits subtle information detail that may not be so pronounced in one image or the other.

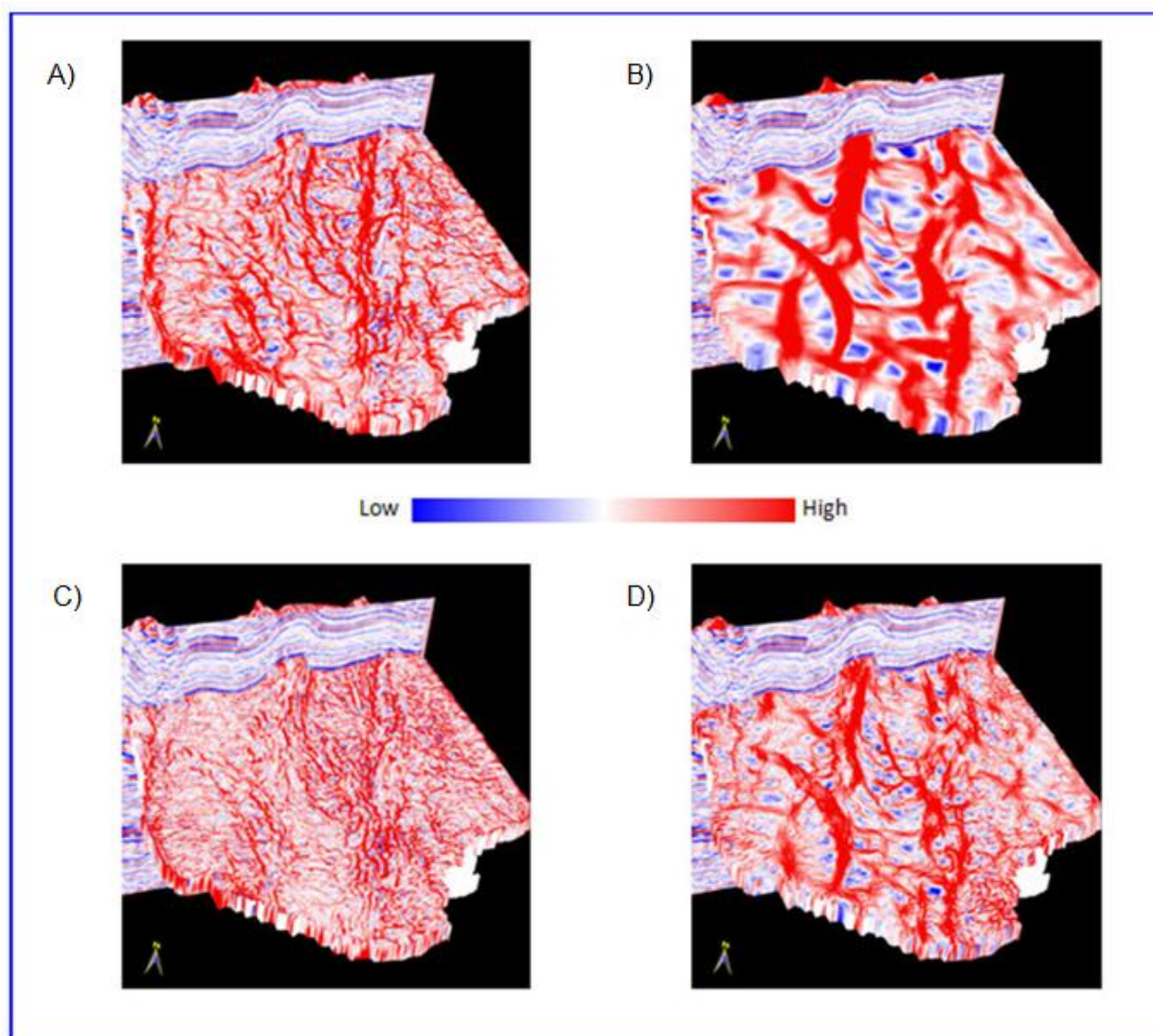


Figure 3. 3D chair views show the seismic inline and strat-cubes from (A) most-positive amplitude curvature (long-wavelength), (B) most-positive structural curvature (long-wavelength), (C) most-positive amplitude curvature (short-wavelength), and (D) most-positive structural curvature (short-wavelength). Notice the higher level of detail on both the amplitude curvature displays as compared with the structural curvature displays.

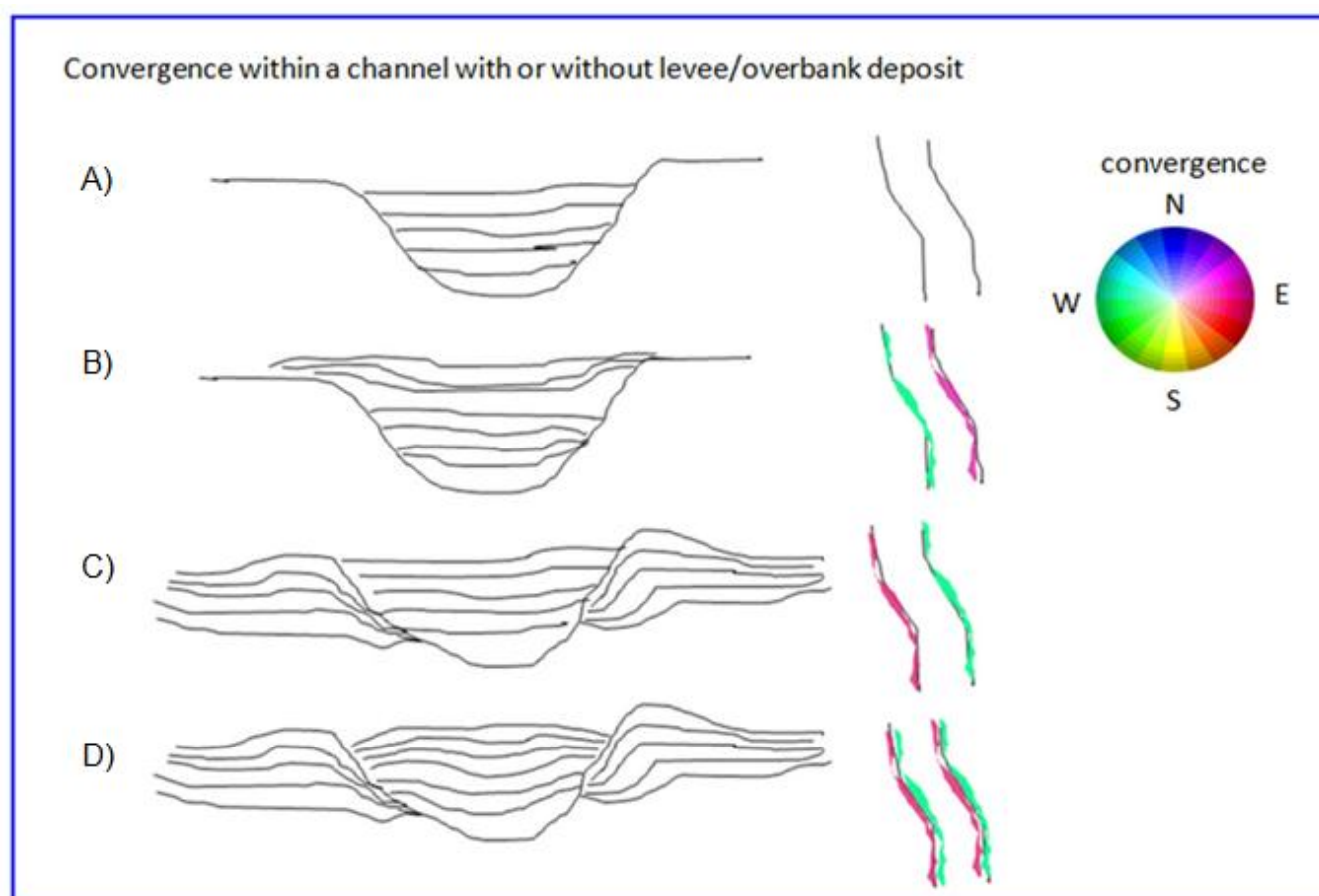


Figure 4. Cartoons demonstrating convergence within a channel with or without Levee/overbank deposits. (A) deposition within the channel shows no significant convergence; (B) shows strata within the channel where the west channel margin converging towards west and the east channel margin converging towards the east. This is displayed in color to the right with the help of a 2D color wheel; (C) shows deposited sediments within the channel not converging at the margins, but the levee/overbank deposits converge towards the channel (west deposits converge towards the east and vice-versa); (D) shows a combination of (B) and (C) where both the strata within the channel and levee/overbank deposits are converging. Notice how the convergence shows up in color as displayed to the right in cyan and magenta colors. (Model and graphics courtesy of Supratik Sarkar, OU).

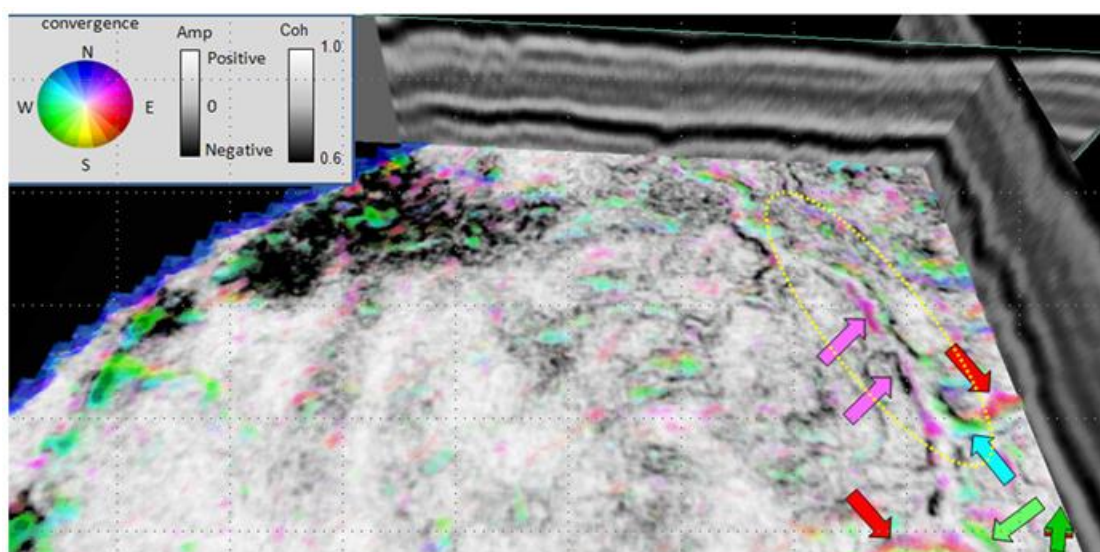


Figure 5. 3D chair view with a coherence time slice as the horizontal section and showing a channel system. This slice is co-rendered with the reflector convergence attribute displayed using a 2D color wheel. Comparing this image to the cartoons in Figure 6, the highlighted ellipse shows a levee/overbank deposit converging towards channel margin generating magenta and green colors with respect to the reflector convergence attribute.

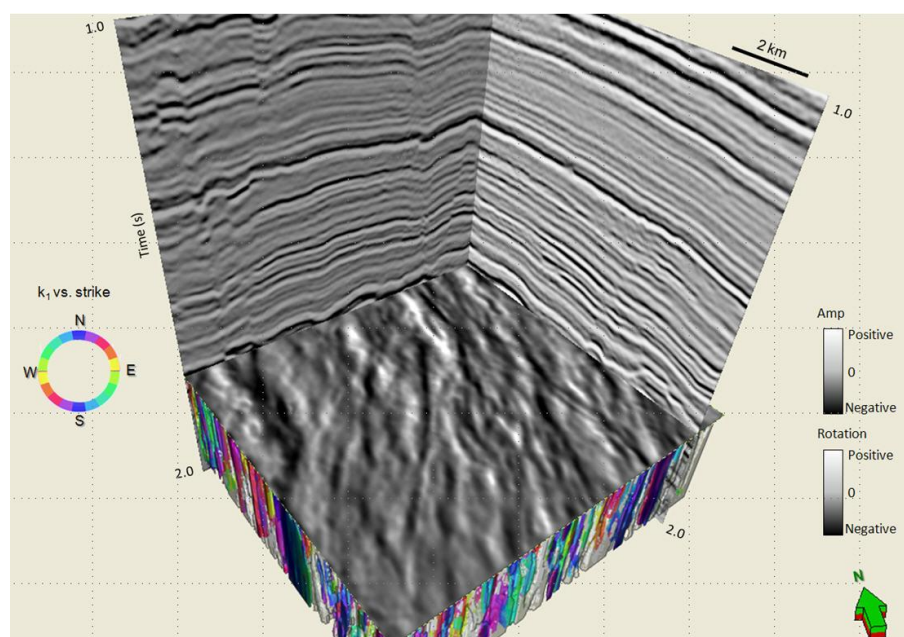


Figure 6. Time slice at $t=1.710$ through a volume of the reflector rotation about the average reflector normal. Not surprisingly, the horst and graben blocks show considerable contrast and can be interpreted as separate units.

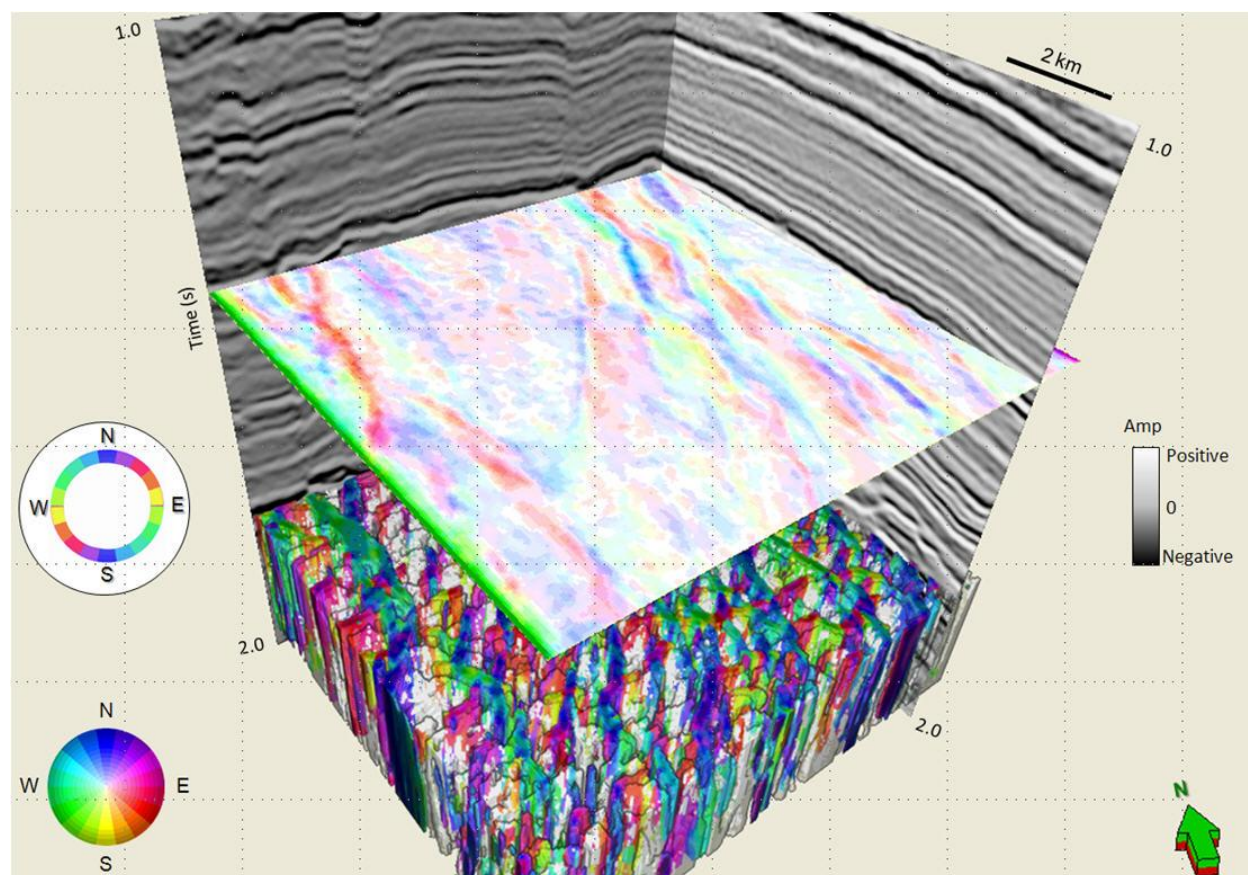


Figure 7. Time slice at $t=1.330$ s through a reflector convergence volume displayed using a 2D color wheel. Blue indicates reflectors pinching out to the North, red to the Southeast, and cyan to the Northwest. Below the time slice we show a box probe view of the most-positive principal curvature lineaments displayed in 3D with the more planar features rendered transparent.